Article

Comprehensive Exploration of Optics and Magnetism in a Hydrothermally Synthesized Nickel(II) Complex

Khouloud Hchicha, Rawia Msalmi, Marcus Korb, Hajir Wahbi,* Erik Čižmár,* Mohamed Hamdi, and Houcine Naïli*

Read Online

ACCESS | Metrics & More | Article Recommendations | SI Supporting Information

ABSTRACT: The hydrothermal reaction of 2-MeIm (2-MeIm: 2-methylimidazole) with nickel sulfate hexahydrate in methanol afforded a mononuclear complex formulated as $[Ni(SO_4)(2\text{-}MeIm)_2(H_2O)_3]\cdot CH_3OH$ (1). The title compound was described by X-ray single-crystal diffraction, thermal assessment, IR, and UV−vis spectroscopy. The crystal structure of **1** is composed of segregated $[Ni(SO_4)(2\text{-}MeIm)_2(H_2O)_3]$ neutral entities and a solvent methanol molecule. Two (2-MeIm) ligands, a sulfate group, and a water molecule reside in the equatorial positions of the vertices in this 6-fold coordination. Two aqua ligands lay in the apical positions, resulting in a subtly distorted octahedral framework, as was supported by spectroscopic analysis. The complex's self-assembly is firmly governed by robust O−H⋯O/N−H⋯O interactions. Further details on these bonds have been furnished via Hirshfeld surface scrutiny and 2D fingerprint plots. As proven by TGA/DSC analysis, raising the temperature of **1** above 60 °C instigates progressive decomposition stages, which culminates in the production of metal oxide as the ultimate product at 700 °C. The optical analysis suggests the dielectric nature of the material with large direct and indirect gap energies of 5.25 and 4.96 eV, respectively. The results of magnetic studies suggest that **1** undergoes a transition to a magnetically ordered state below 6 K.
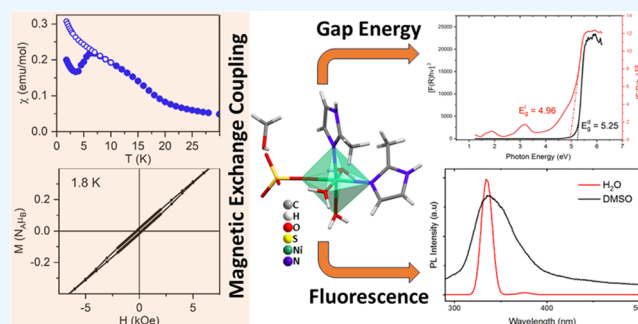
1. INTRODUCTION

Hydrothermal reactions guarantee favorable routes for the preparation of novel metal-containing complexes with highly thermodynamically stable phases and intriguing structural configurations, imparting them with alluring characteristics[1,2] applicable in potential applications such as superionic conductors,[3] chemical sensors,[4] electronic conduction,[5] luminescence phosphors,[6] and magnetism.[7] Nevertheless, controlling the formation and structure types of the produced complexes remains an arduous and daunting task. Countless studies have demonstrated that the use of N-donor heterocyclic ligands yields a profusion of structurally diversified multifunctional materials.[8−16] Among an extensive array of N-donor heterocyclic ligands, imidazole and its derivatives have triggered considerable attention for being a prominent structural constructor owing to their high affinity to metal, amphoteric character, and their ability to create hydrogen bonds and π−π* interactions. Imidazole-bearing complexes raise the interest of researchers not only from a structural point of view but also from their efficiency in a plethora of pharmacological and biological processes, as already proven in various studies, viz. antiprotozoal, antifungal, antioxidant, antimicrobial, antibacterial, and antitumor properties. Furthermore, they have witnessed their effectiveness as catalysts in the oxidation of cyclohexane,[17] 4-nitrophenol reduction,[18] and

Suzuki−Miyaura and Sonogashira Coupling Reactions.[19] Previous studies have also reported some imidazole-containing complexes to possess dominant antiferromagnetic interactions and ferromagnetic coupling.[20,21] In addition, some exhibit interesting luminescence properties.[22]

Taking inspiration from the aforementioned points, we hydrothermally synthesized a new imidazole-based complex utilizing both 2-methylimidazole and nickel sulfate hexahydrate that was anticipated to afford distinct arrangement, with entrancing properties.

In pursuit of an accurate structural depiction, an apt structural examination is conducted in conjunction with Hirshfeld surface scrutiny, accompanied by spectroscopic, thermal, optical, and magnetic assessments.
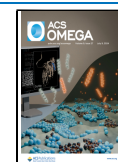
2. EXPERIMENTAL SECTION

2.1. Materials and Physical Measurements. All of the chemicals were employed as received without additional

purification. Nickel(II) sulfate hexahydrate and 2-methylimi-dazole were procured from Sigma-Aldrich.

Infrared measurements were undertaken at room temperature using KBr pellets in the range 400−4000 cm⁻¹ with a Bruker Optics Vertex 70 FT-IR spectrophotometer.

Thermal analyses (combining TGA with DSC) were carried out using a Mettler Toledo 1100 system with a UMX1 balance on a 9.48 mg sample within the 40−800 °C temperature range with a heating rate of 10 K/min under an argon atmosphere.

The absorption spectra in solutions were recorded using a Hewlett-Packard 8452A spectrophotometer in 1×10^{-5} M water and DMSO solutions. Fluorescence spectra were measured on a Xenius SAFAS spectrofluorometer in water and DMSO (1×10^{-6} M) solutions.

Solid-state optical behavior was studied using diffuse reflectance measurements performed on a Varian Cary 5000 UV−vis-NIR spectrophotometer operating at room temperature in the 200−1000 nm region.

Susceptibility (derived from the ratio of the measured magnetic moment to the applied magnetic field) and magnetization measurements were conducted on a commercial Quantum Design MPMS-XL5 magnetometer. An incipient polycrystalline sample was enclosed in a gelatin capsule fastened to a long, uniform straw (not contributing to the measured magnetic moment). First, the sample was cooled down in the zero-magnetic field, a small magnetic field of 1 kOe was implemented, and the magnetic moment was assessed during the warming up from 1.8 to 300 K. Then, the sample was cooled back in the same applied field and magnetic moment measured again. The magnetic moment of the gelatin capsule obtained from the independent measurements was subtracted from the measured magnetic moment. Subsequently, the diamagnetic susceptibility of the sample itself was estimated using Pascal's constants and subtracted.

2.2. Computational Details. Ab initio calculations were performed using the ORCA 5.0.1 computational package.[23] The crystal field parameter calculations were based on the state-averaged complete-active-space self-consistent field (SA-CASSCF) wave functions followed by N-electron valence second-order perturbation theory (NEVPT2).[24−28] The active space of the CASSCF calculations on metal-based d-orbitals of Ni(II) ions was set as CAS(8,5) and CAS(8,10). All 10 triplet and 15 singlet states equally weighted were included in the state-averaged approach. The zero-field splitting (ZFS) parameters were then calculated through the quasi-degenerate perturbation theory,[29] in which an approximation to the Breit−Pauli form of the spin−orbit coupling operator[30] and the effective Hamiltonian theory was utilized.[31]

Relativistic effects were taken into account by using the zeroth-order regular approximation[32,33] using segmented all-electron relativistic contracted (SARC) version of the triple-ζ basis set Def2-TZVP[34] for all atoms. The calculations utilized the RI approximation and the chain-of-spheres (RIJCOSX) approximation to exact exchange[35] and appropriate decontracted auxiliary basis sets.[36,37] Tight SCF convergence criteria were used in all calculations. Positions of hydrogen atoms in the model molecule were optimized by the DFT method using the B3LYP functional. The atom-pairwise dispersion correction with the Becke−Johnson damping scheme (D3BJ)[38,39] was included. The SARC def2-SVP basis set was used for hydrogen and carbon atoms in the DFT calculations.

2.3. X-ray Data Collection. Diffraction data for complex **1** were obtained at 120 K by using an Oxford Gemini S diffractometer. The determination of unit cell parameters and data collection utilized a graphite monochromatic Mo $K\alpha$ (λ = 0.71073 Å) radiation source. The molecular solid-state structure was resolved via direct methods and refined with full-square methods on F² using SHELXS/SHELXL-2013 in the WinGX interface.[40] Positions of all non-hydrogen atoms were determined directly. C-bonded hydrogen atoms were geometrically fixed at determined positions and treated as riding on their parent atoms, and a riding model was used in the treatment of the hydrogen atom positions. The NH hydrogen atoms were set up from the inspection of the difference Fourier maps and coerced using DFIX 0.870 and 0.010. Crystal data and refinement results are summarized in Table 1, and molecular graphics were generated using the
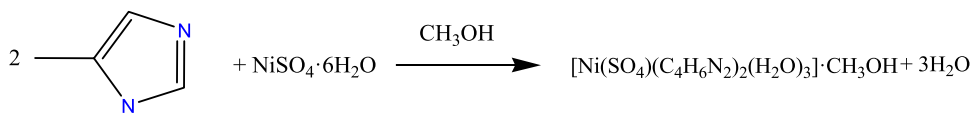
Table 1. Crystallographic and Structure Refinement Data for 1

structural parameters	compound (1)
empirical formula	$C_9H_{22}N_4O_8SNi$
formula weight (g mol⁻¹)	405.07
temperature (K)	120
crystal system	monoclinic
space group	$P2_1/n$
a (Å)	7.5024 (5)
b (Å)	16.9691 (10)
c (Å)	14.3776 (10)
β (deg)	99.837(7)
volume (Å³)	1803.5 (2)
Z	4
diffractometer	Oxford Gemini S
ρ_{cal} (mg m⁻³)	1.492
absorption correction	semiempirical from equivalents
crystal size (mm³)	0.4 × 0.2 × 0.02
crystal color/shape	block, pale green
μ (mm⁻¹)	1.233
hkl range	$-8 \leq h \leq 8$
	$-20 \leq k \leq 19$
	$-17 \leq l \leq 17$
no. of reflections collected	100 63
no. of independent reflection	3130
F (000)	848
R_1	0.0520
wR_2	0.1224
GooF	1.039
transmission factors	T_{min} = 0.95569, T_{max} = 1.00000
largest difference map hole	$\Delta\rho_{min}$ = −0.437 e Å⁻³; $\Delta\rho_{max}$ = 1.231 e Å⁻³

DIAMOND program.[41] Crystallographic data are accessible in the Supporting Information and deposited at the Cambridge Crystallographic Data Centre.

To corroborate the structural findings, the powder X-ray diffraction (XRD) pattern was documented (Figure S1). The alignment observed between the experimental and simulated patterns verifies the phase integrity of the material obtained.

2.4. Hirshfeld Surface Analysis. To explore and quantify the intermolecular interactions in our compound, Hirshfeld surface (HS) analysis was achieved. 3D HS and 2D fingerprint plots (FP) are generated by importing the structure of the crystallographic information file (CIF) in CrystalExplorer software (version 3.1)[42] as an input file. The HS is constructed based on the electron distribution that is assessed using (d_{norm}) given by this formula:

Scheme 1. Reaction Scheme of the Synthesis of the Complex $[Ni(SO_4)(2\text{-}MeIm)_2(H_2O)_3]\cdot CH_3OH$ (1)

$$2 \quad \text{(2-methylimidazole)} + NiSO_4 \cdot 6H_2O \xrightarrow{\ CH_3OH\ } [Ni(SO_4)(C_4H_6N_2)_2(H_2O)_3] \cdot CH_3OH + 3H_2O$$

$$d_{\text{norm}} = \frac{d_i - r_i^{\text{vdw}}}{r_i^{\text{vdw}}} + \frac{d_e - r_e^{\text{vdw}}}{r_e^{\text{vdw}}} \tag{1}$$

where d_{norm} stands for the normalized contact distance, which permits the pinpointing regions of particular significance to the intermolecular interactions, d_i is the distance from a point on the surface to the nearest internal nucleus, d_e is the distance from a point on the surface to the nearest nucleus external to the surface, and r_i^{vdw} and r_e^{vdw} correspond to the van der Waals radii of the atoms.

Within a scientific framework, a color spectrum spanning from red (indicating distances shorter than van der Waals separation) to blue (indicating distances longer than van der Waals separation) is utilized to highlight significant areas in the dnorm map.

3. SYNTHESIS PROCESS, RESULTS, AND DISCUSSION

3.1. Synthesis Process. Compound 1 was synthesized via a hydrothermal procedure in a sealed Teflon-coated stainless-steel autoclave under autogenous pressure, which contains nickel(II) sulfate hexahydrate and 2-methylimidazole in a molar ratio of 1:2, and 7 mL of methanol. Then, it was placed inside a programmable stove and subjected to heating for 24 h at 140 °C (with a heating rate of 5 °C/min). Subsequent cooling of the autoclave to 100 °C at the same rate was followed by a 24 h incubation period at this temperature before gradual cooling to room temperature at a rate of 2 °C/min. The resulting pale green crystals were separated via filtration, washed, and recrystallized from methanol. The yield of this synthesis method was around 84%. The reaction scheme of the synthesis of complex 1 is given below (Scheme 1).

The elemental analysis was carried out to validate the composition of complex 1. The outcomes indicated the presence of H: 5.335(3)% (theor. 5.436%), C: 26.515(2)% (theor. 26.687%), N: 13.742(2)% (theor. 13.837), O: 31.743(3)% (theor. 31.629), and S: 8.112(2)% (theor. 7.907). These experimental results strongly corroborate the molecular formula of the complex, confirming its precise composition and structural stability.

4. RESULTS AND DISCUSSION

4.1. Infrared Spectroscopy. According to the literature, IR characteristic bands were tentatively assigned (Figure 1). The broad peaks observed in the range $[3500-3200]$ cm^{-1} are assignable to the O—H stretching vibration of methanol and water molecules. The weaker ones around 3136-3156 cm^{-1} are typical for the stretching vibration of C—H in the imidazole ring together with $\nu(N-H)$ of the secondary amine group, proving the neutrality of the organic ligand.[43] The relatively faint peaks between the 2800 and 3000 cm^{-1} spectral range represent the methyl group of 2-MeIm. The band around 1648 cm^{-1} corresponds to vibrational mode $\nu(C=N)$. Compared to the spectra of the free organic ligand, this band is shifted toward lower wavenumbers, which denote its coordination with the metal through a pyridine-type nitrogen atom.[44] The C—C and C—N stretch vibrations of the 2-MeIm appear
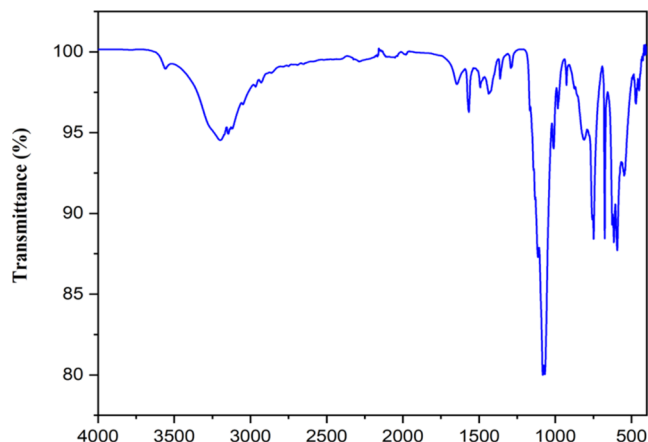

Figure 1. Infrared spectra of 1 (KBr pellet).

between the 1400 and 1600 cm^{-1} range. Stretching vibration modes of the 2-MeIm ring are detected in the wavenumber range $[1100-1400]$ cm^{-1}, while deformation vibration modes are observed in the range $[650-850]$ cm^{-1}. The strong band around 750 cm^{-1} corresponding to vibration mode $\rho_r(H_2O)$ proves the involvement of the water molecules in the coordination environment of the nickel complex.[45] Alongside the mentioned typical bands for the organic ligand and the water molecules, three bands appear at 970, 1111, and 630 cm^{-1}, assignable to ν_1, ν_3, and ν_4 of $(-SO_4)$ group in a (C_{3v}) symmetry, confirming its monodentate coordination.[46]

Therefore, the IR data are significantly consistent with the results obtained from the crystallographic data.

4.1.1. Thermal Behavior. As can be seen in Figure 2, the thermal decomposition initiates at 60 °C with the liberation of the methanol and three water molecules with a calculated mass loss of 21.2% (exp 21.1%), coinciding with an endothermic peak on the DSC curve. The resulting anhydrous compound is thermally stable until 280 °C, and then two (2-MeIm)
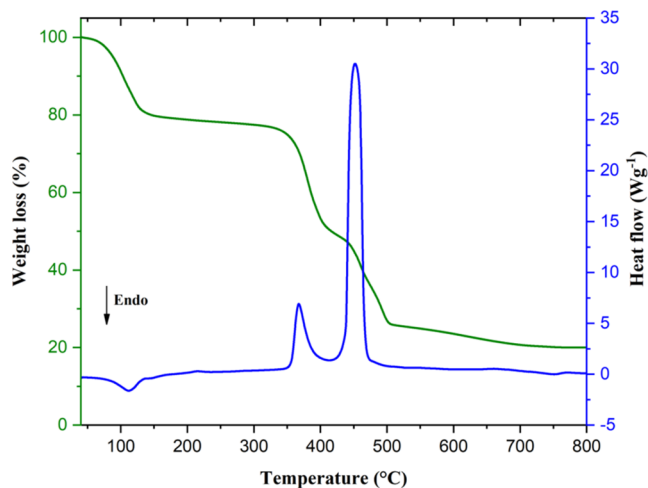

Figure 2. Simultaneous TG-DTA curves for the decomposition of 1.

molecules are released in an oxidative degradation between 280 and 410 °C as two overlapped processes associated with an exothermic effect (calc. mass loss 40.5%, exp. 40.2%). Continued heating of the remainder of the complex results in the loss of the sulfate group, producing a strong exothermic effect (calc. mass loss 23.7%, exp. 22.8%). Ultimately, thermal decomposition above 700 °C is anticipated to produce nickel oxide (NiO).

4.1.2. Crystal Structure Determination. The molecular arrangement of **1** (Figure 3) consists of a [Ni(SO$_4$)(2-MeIm)$_2$(H$_2$O)$_3$] neutral entity and a solvate methanol molecule. The crystalline form belongs to the monoclinic P2$_1$/n space group.
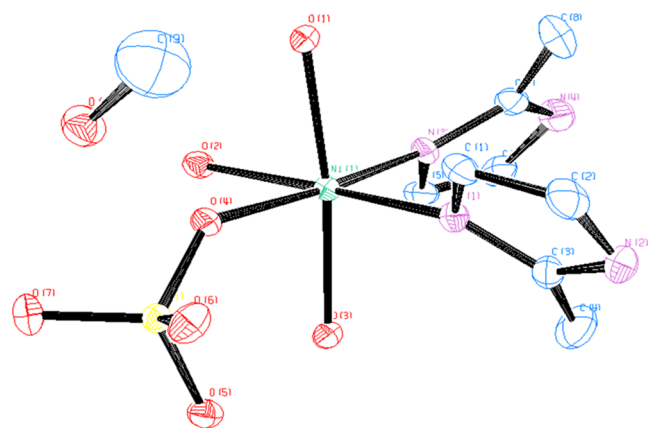

Figure 3. ORTEP representation (at a 50% probability level) showcases the asymmetric unit of the molecular structure of **1**, alongside the atom numbering scheme. For clarity, hydrogen atom labels have been left out.

More in-depth information about bond lengths (Å), bond angles (deg), and torsion angles (deg) is listed in Table S1.

Two distinct 2-MeIm ligands, three water molecules, and a sulfate group ligate the nickel(II) center to construct a slightly distorted octahedron, as indicated by the values of the angles (N1−Ni−N3= 93.961(2)°, O2−Ni−O4= 85.225(2)°, O4−Ni−N1= 89.600(2)°, and O2−Ni−N3= 91.202(2)°). Two oxygen atoms of the water molecules occupy the axial positions (O3−Ni−O1= 171.842 (2)°), while the equatorial plane is built up with the third water molecule, the sulfate anion plus two nitrogen atoms from the organic ligand. As can be seen in Figure 3, the nitrogen atoms of the amine are *cis* to each other, with a *fac*-disposition of the aqua ligands. The angle formed between the two imidazole rings is measured at 55.394°. The central ion is practically located in the equatorial plane with a deviation of −0.0294 Å. The bond angles around the Ni-center range from 89.600(2)° to 171.842(2)°; Ni−N bond lengths are equal to 2.046(4) and 2.053(4) Å, while the Ni−O bond lengths vary from 2.083(3) to 2.114(3) Å. Those values align well with those observed in other hexacoordinated nickel imidazole analogues.[47,48]

The packing of the different molecular entities is shown in Figure 4; the projection along the *a*-axis discloses a supramolecular layered structure built of an alternate stacking of organic layers, between which the inorganic units were intercalated. The closest Ni···Ni spacing is 5.1621(2) Å. A labyrinthine network of hydrogen bonds guarantees the connectivity of the various constituents within the crystal lattice (Table S2). The methanol molecule participates via its
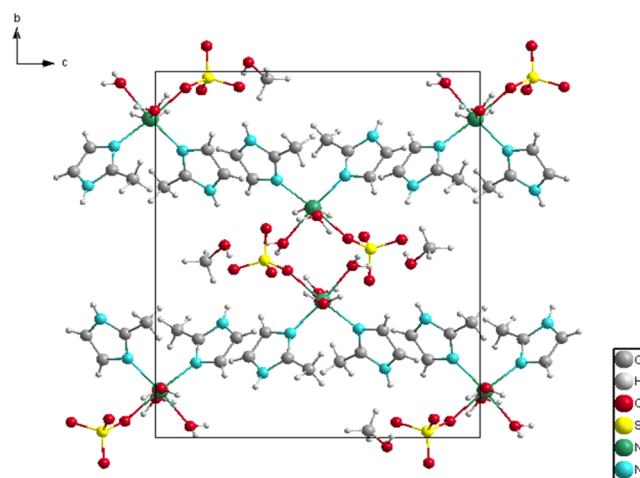

Figure 4. Packing of **1** along the crystallographic *a*-axis.

hydroxyl group hydrogen-bonded to the N atom of the organic ligand, conjointly with its interactions with water molecules and the sulfate group. O1 and O3 act as bifurcated donors with O4, O7, and O4, O2, respectively. Conversely, atoms O8, O5, O6, and O7 partake in bifurcated acceptor interactions. Thus, all oxygen and noncoordinated nitrogen atoms in **1** engage in intermolecular interactions, resulting in a robust hydrogen-bond network. Supplementary C−H···π interactions (Figure S2), created between the organic ligands, complement the stability of the packing toward 3D assembly.

4.1.3. Hirshfeld Surface Analysis. Figure 5 showcases a visualization of the three-dimensional Hirshfeld surface for compound 1, where the normalized contact distance is plotted against the electrostatic potential energy range from −0.7101 to 2.4247 atomic units.

The bright-red circular spots on the d_{norm} surface highlight the predominance of O−H···O hydrogen bonding of the O−H···O ions arising from the interaction of the coordinated water molecules and the sulfate group with neighboring molecules.

The generated 2D fingerprint plots (Figure S3) consistently underline the preponderance of H··H and O··H/H··O intermolecular contacts in the crystal stability, accounting for 49.6 and 41.3% of the total HS, respectively. The C··H-π interactions, referred to as C··H interactions and depicted as a wing pair in the FP, represent 4.7% of the contribution. Additionally, the existence of those interactions can be evidenced on the HS mapped over the shape index (Figure S4), showing intense red spots above the (2-MeIm) ring system and blue blots adjacent to the C··H donor.

Moreover, certain other interactions with minor quantitative involvement in sustaining the crystal packing are observed, such as H··N/N··H (1.5%), C··C (1.1%), and C··N/N··C (1%) contacts. A summary of the main intermolecular contacts contributing to the supramolecular assembly is illustrated as a histogram in Figure 6.

4.2. Optical Properties. *4.2.1. Absorption Properties.* The solid-state diffuse reflectance spectrum of the synthesized complex was recorded between 200 and 1000 nm. According to Kubelka−Munk (K−M) function (eq 1, where R is the sample reflectance),[49,50] the reflectance spectrum has been transformed into absorption spectrum F(R) (Figure 7). The UV−vis spectrum of the investigated complex bears a resemblance to the absorption spectra of octahedral Ni(II)
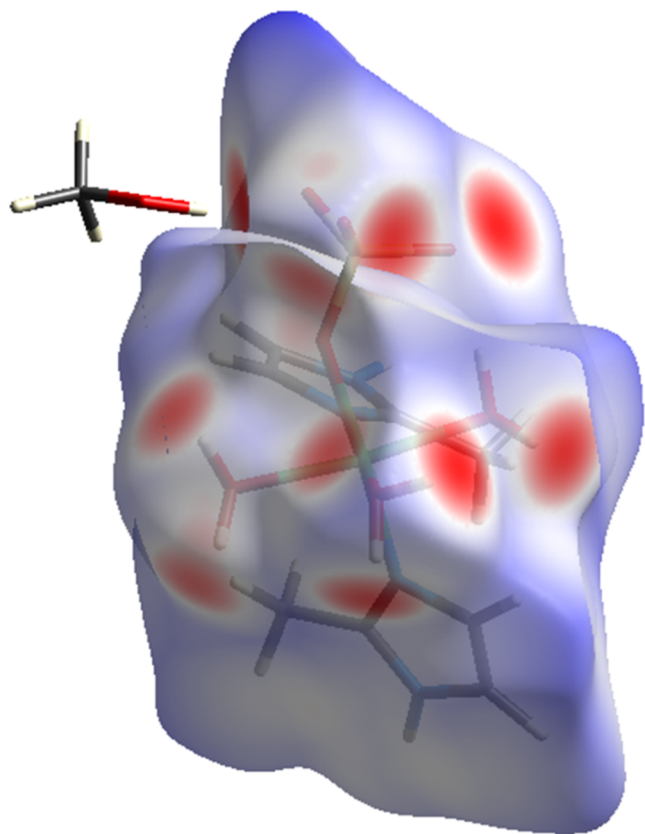
Figure 7. K-M absorption spectra of **1**.

dependence of the observed d−d transition energies on the donor stets and then on the symmetry site of the Ni^{2+} ions.

The best multipeaks fitting of the absorption bands observed above 550 nm (Figure 8) shows the existence of three d−d

Figure 8. Three peaks Gaussian fitting of the d-d transitions within **1**.

transitions around 655 nm (15 267 cm^{-1}), 748 nm (13 368 cm^{-1}), and around 1018 nm (9823 cm^{-1}). Such observed transitions are characteristic of Ni(II) complexes with N_2O_4 coordination spheres, where the NiN_2O_4 octahedra have elongated D_{4h} geometry.[51] According to the similar Ni(II) complexes previously reported, the NiN_2O_4 polyhedron displays six triplet−triplet d-d transitions.[51,55,56] For the $[Ni(CMA)_2(Im)_2(MeOH)_2]$[57] (CMA = 9,10-dihydro-9-oxo-10-acridineacetate ion), where Ni−N and Ni−O distances of the NiN_2O_4 octahedron are close to those of our complex, four d−d transition bands are observed at about 16 020, 13 855, 10 770 and 8220 cm^{-1}. These bands are assigned to transitions from the ground-state $^3B_{1g}$ to ^3E_g ($^3T_{2g}-O_h$), $^3A_{2g}$, $^3B_{2g}$ and ^3E_g ($^3T_{1g}-O_h$), respectively.[51]

The direct and indirect fundamental bandgap energies of the synthesized complex have been investigated using the Tauc relation (eq 2).

$$[F(R) \times h\nu]^{1/m} = A(h\nu - E_g) \qquad (3)$$

where A stands for a constant, h represents Planck's constant, and ν denotes the photon frequency.

The graph of $[F(R)h\nu]^2$ and $[F(R)h\nu]^{1/2}$ vs $h\nu$ (Figure 9) shows that **1** is particularized by direct and indirect gap energy of 5.25 and 4.96 eV, respectively. This large gap value confirms the dielectric property of the synthesized complex and makes it suitable for optoelectronic applications.[58−60]

Figure 5. Hirshfeld surface mapped with d_{norm} around the asymmetrical unit of **1**.
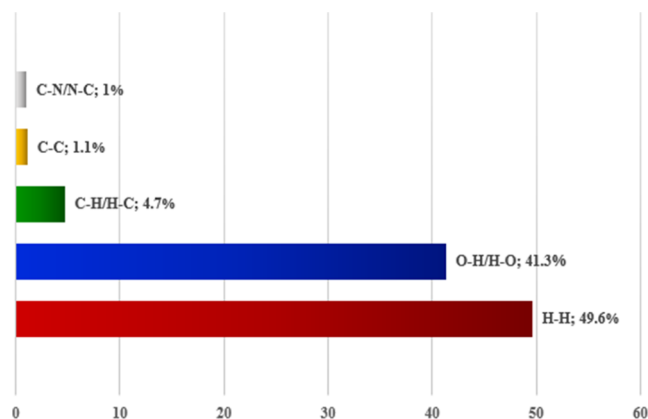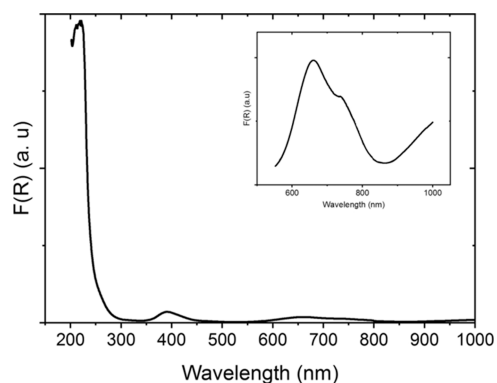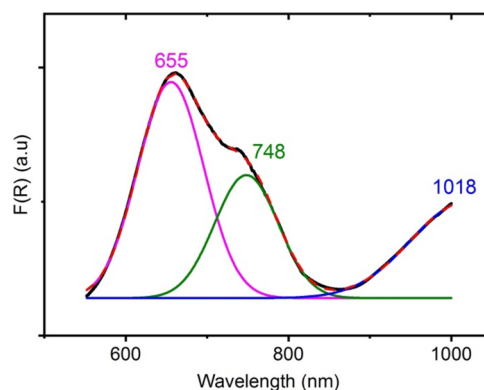

Figure 6. Proportional impacts of intermolecular interactions on the Hirshfeld surface area for **1**.

complexes with N, O donors.[51−53] The material displays an intense absorption band below 250 nm and a low band around 391 nm resulting from Ligand−Ligand charge transfer (LLCT) and Ligand−Metal charge transfer (LMCT), respectively.

$$F(R) = \frac{(1 - R)^2}{2R} = \frac{K}{S} \qquad (2)$$

As shown in the inset of Figure 7, the spectrum displays broad absorption bands between 545 and 1000 nm, which originate from the d−d transitions within the Ni^{2+} cations. Spellbinding research on electronic structures of octahedral Ni(II) complexes with N_2O_4,[51] N_3O_3, N_4O_2, and N_6[54] donor sets has been reported. All of these studies substantiated the
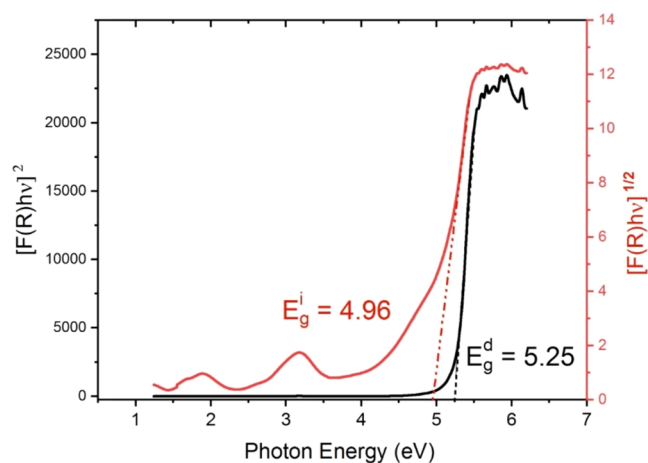
Figure 9. Tauc plots of the direct and indirect gap energies.

To scrutinize the impact of the solvent on the absorption properties of **1**, we recorded the absorption spectra in H_2O and DMSO solutions. As shown in Figure 10, the absorption in
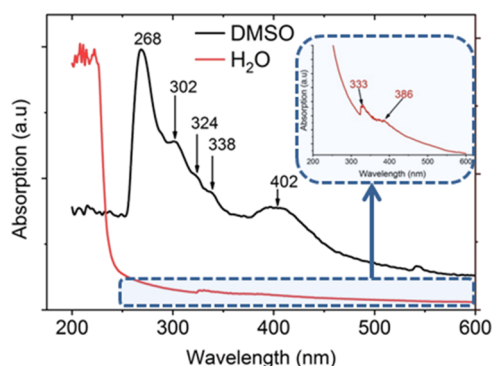

Figure 10. Absorption spectra of **1** in water and DMSO.

water closely resembles that in the solid state. However, in DMSO, the intense band observed in the UV region resulting from LLCT is shifted to the highest wavelengths with deconvolution of different electronic transitions that contributed to this band. The absorption spectrum in DMSO is comparable to that of octahedral nickel(II) complex with N_2O_4 donors, $[\{NiL(MeOH)(l\text{-}OAc)\}_2Ni]\cdot 4CH_2Cl_2$, that has been measured in dichloromethane solutions.[53]

4.2.2. Photoluminescence Properties. The photoluminescence spectrum of **1** has been recorded in water and DMSO under an excitation wavelength of 222 and 268 nm, respectively. As depicted in Figure 11, in DMSO, the complex exhibits a broad emission centered at 336 nm, which is observed at 357 and 365 nm in the previously reported Ni(II) complexes.[61] This band was attributed to the $\pi-\pi^*$ transition. In water, our compound exhibits two emission bands at around 334 and 377 nm.

4.3. Magnetic Properties and Theoretical Calculations. The magnetic properties of **1** were studied in the temperature range between 1.8 and 300 K. The room-temperature value of $\chi T = 1.34$ emuK/mol (the effective magnetic moment $\mu_{eff} = 3.28\ \mu_B$, where μ_B is Bohr magneton) is typical for Ni(II) ions ($3d^8$, spin $S = 1$) in the paramagnetic limit. The temperature dependence of the χT product of **1** in Figure 12 shows an increase with the lowering temperature, followed by a steeper decrease down to the lowest temper-
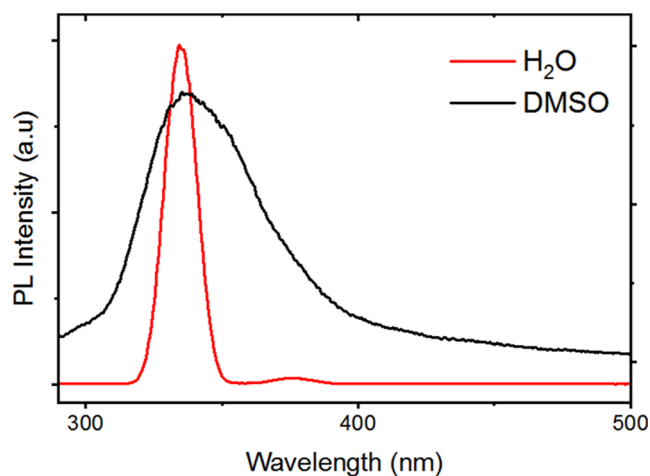

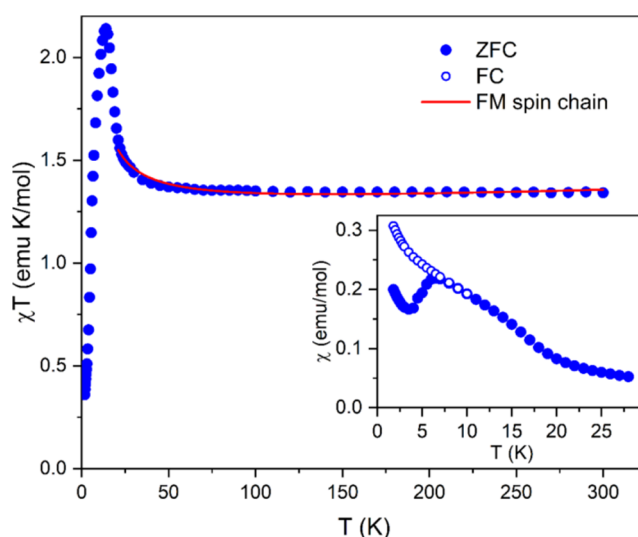**Figure 11.** PL spectrum of **1** under $\lambda_{exc} = 222$ nm.

Figure 12. Temperature dependence of the χT product of **1** (symbols) in the ZFC regime, including the fit of the FM spin chain model in the high-temperature region (solid red line) at temperatures above the magnetic ordering. The inset shows the ZFC and FC susceptibility behavior with the magnetically ordered state suggested below 6 K.

atures. A difference between zero-field-cooled (ZFC) and field-cooled (FC) magnetic response was observed in the magnetic susceptibility, measured in the applied magnetic field of 1 kOe, shown in the inset of Figure 12 below 7 K. The ZFC susceptibility subsequently dropped below 6 K.

A hysteretic behavior was then observed in the field dependence of the magnetization at 1.8 K with a coercive field of 300 Oe, as shown in the inset of Figure 13 as an indication of long-range magnetic order. An increase of the χT could not be associated with the presence of isolated Ni(II) ions only in **1** described by the spin Hamiltonian, which includes an axial ZFS parameter D and a rhombic parameter E. A ferromagnetic (FM) exchange coupling between the Ni(II) centers must be considered due to an extensive network of hydrogen bonds mediating the exchange coupling. Besides, the drop in susceptibility below 6 K could be explained by the competition between the major FM and an additional antiferromagnetic (AFM) exchange coupling. The presence of a relatively strong exchange coupling mediated by hydrogen
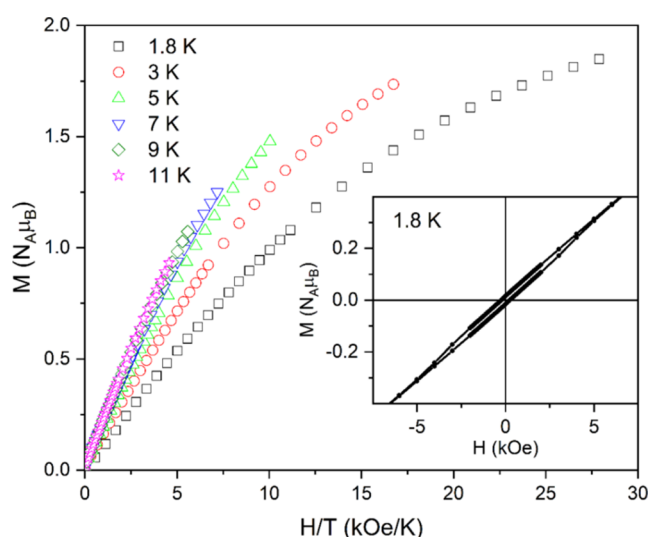
Figure 13. Initial magnetization curves of **1** (symbols) in rescaled coordinates measured at several temperatures. The inset shows the hysteresis of the magnetization loop observed at 1.8 K.

bonds in Ni(II) coordination complexes is not unusual, e.g., in.[62] The field dependence of the magnetization measured at different temperatures was plotted in the rescaled coordinates in Figure 13. The deviation between magnetization curves in Figure 13 over the whole field range suggests an interplay of the exchange coupling and magnetic anisotropy described by the spin Hamiltonian; if FM coupling was only taken into account, the curves would tend to meet at high H/T at low temperatures.

To assess the ZFS parameters, ab initio calculations were performed in the ORCA on isolated neutral $[Ni(SO_4)(2\text{-}MeIm)_2(H_2O)_3]$ molecules. The SA-CASSCF/NEVPT2 calculations using the atom positions estimated from X-ray diffraction are summarized in Table 2. The positions of hydrogen atoms were optimized using the DFT method before such calculations. The obtained values suggest that ZFS in **1** is characterized by the easy-plane type of anisotropy ($D > 0$) with a relatively large rhombic contribution. Usually, ZFS parameters and exchange couplings are highly correlated in the analysis of magnetic response, and several experimental methods need to be implemented to assess all parameters accurately, as shown in.[63,64] No simple formula for the susceptibility (or magnetization) analysis is available to account for the complicated exchange-coupling network mediated by hydrogen bonds and ZFS in **1**. The main exchange path could be forming spin chains along the crystallographic a-axis through H_2O and SO_4 groups or along the crystallographic c-axis through 2-MeIm ligands. Therefore, the high-temperature part of the susceptibility well above the magnetic ordering was analyzed using an anisotropic $S = 1$ FM chain model with Hamiltonian in the form of $-J\sum_i S_i S_{i+1}$ derived by Fisher[65] as

$$\chi_{chain} = \frac{N_A g^2 \mu_B^2 S(S+1)}{3k_B T} \frac{1+u}{1-u} \tag{4}$$

$$u = \coth \frac{JS(S+1)}{k_B T} - \frac{k_B T}{JS(S+1)} \tag{5}$$

with exchange-coupling constant J, Avogadro constant N_A, and Boltzmann constant k_B. The predicted D value of about 5 K and additional AFM correlations may be neglected at sufficiently high temperatures. A contribution of the temperature-independent paramagnetism and a possible correction to the estimation of diamagnetic susceptibility of the sample was included as $\chi = \chi_{chain} + \chi_0$. A fit of the temperature dependence of the χT in Figure 12 yielded the estimate of a dominant FM exchange-coupling $J/k_B = 3.25$ K with an average g-factor $g = 2.242$ and $\chi_0 = 2.7 \times 10^{-4}$ emu/mol. Further high-frequency electron paramagnetic resonance or inelastic neutron scattering experiments on sufficiently large single crystals are possibly necessary to estimate the parameters accurately.

5. CONCLUSIONS

To summarize, a novel imidazole-based complex was effectively synthesized. Its crystal arrangement was solved and refined from X-ray diffraction data, which shows that the asymmetric unit incorporates one crystallography-independent $[Ni(SO_4)(2\text{-}MeIm)_2(H2O)_3]$ fragment and a solvent methanol molecule. The central Ni(II) metal ion is coordinated by two nitrogen atoms derived from two neutral (2-MeIm) ligands, a sulfate group, and a water molecule in the equatorial plane of a distorted octahedron, whose coordination sphere is completed by two aqua ligands occupying the axial positions. The great number of potential hydrogen-bond donors and acceptors in **1**, i.e., two N—H groups and three noncoordinated sulfate oxygen atoms, H_2O, and MeOH molecules, enables the formation of a rigid hydrogen-bonding network. Additional weak intermolecular C—H···π contacts established among the organic ligands enhance the rigidity of the complex. A thermal study reveals that **1** undergoes three decomposition steps, leading to the metal oxide as a final expected product. The optical analysis suggests the dielectric nature of the material with large direct and indirect gap energy of 5.25 and 4.96 eV, respectively. The photoluminescence response of **1** in water and DMSO shows ultraviolet emission. The examination of the magnetic results implies the presence of a relatively strong exchange coupling mediated by hydrogen bonds in **1**, which yields magnetic ordering at temperatures below 6 K.

■ ASSOCIATED CONTENT

ⓢ Supporting Information

The Supporting Information is available free of charge at https://pubs.acs.org/doi/10.1021/acsomega.4c00421.

> Selected bond geometries, hydrogen bond properties, PXRD patterns, 2D fingerprint plots, and Hirshfeld surfaces for **1** (PDF)

Table 2. Comparison of the Spin Hamiltonian Parameters for 1 Derived from SA-CASSCF/NEVPT2 Calculations Done in ORCA

	D/k_B [K]	E/D	g_1	g_2	g_3	g_{avg}
$[Ni(SO_4)(2\text{-}MeIm)_2(H_2O)_3]$ CAS(8,5)	4.65	0.153	2.213	2.234	2.242	2.230
$[Ni(SO_4)(2\text{-}MeIm)_2(H_2O)_3]$ CAS(8,10)	5.10	0.142	2.238	2.262	2.270	2.257
experiment						2.242

Crystallographic data are accessible in the SI and deposited at the Cambridge Crystallographic Data Centre (CIF)

■ AUTHOR INFORMATION

Corresponding Authors

Hajir Wahbi − *Department of Chemistry, College of Sciences and Arts, Turaif, Northern Border University, Arar, Saudi Arabia*; Email: Hajir.Wahbi@nbu.edu.sa

Erik Čižmár − *Faculty of Science, Institute of Physics, P.J. Šafárik University in Košice, SK-041 54 Košice, Slovakia*; Email: erik.cizmar@upjs.sk

Houcine Naïli − *Laboratory Physico Chemistry of the Solid State, Department of Chemistry, Faculty of Sciences, University of Sfax, 3000 Sfax, Tunisia*; ⊙ orcid.org/0000-0002-9224-5851; Email: houcine.naili@fss.rnu.tn

Authors

Khouloud Hchicha − *Laboratory Physico Chemistry of the Solid State, Department of Chemistry, Faculty of Sciences, University of Sfax, 3000 Sfax, Tunisia*

Rawia Msalmi − *Laboratory Physico Chemistry of the Solid State, Department of Chemistry, Faculty of Sciences, University of Sfax, 3000 Sfax, Tunisia*

Marcus Korb − *Faculty of Sciences, School of Molecular Sciences, The University of Western Australia, Perth, Western Australia 6009, Australia*

Mohamed Hamdi − *Department of Chemistry, College of Sciences and Arts, Turaif, Northern Border University, Arar, Saudi Arabia*

Complete contact information is available at:
https://pubs.acs.org/10.1021/acsomega.4c00421

Notes
The authors declare no competing financial interest.

■ REFERENCES

(1) Xiang, X.-D.; Vareka, W. A.; Zettl, A.; Corkill, J. L.; Barbee, T. W.; Cohen, M. L.; Kijima, N.; Gronsky, R. Tuning High-Tc Superconductors via Multistage Intercalation. *Science* **1991**, *254*, 1487−1489.

(2) Burkholder, E.; Golub, V.; O'Connor, C. J.; Zubieta. A building block approach to the synthesis of organic−inorganic hybrid materials. *J. Inorg. Chem.* **2003**, *42* (21), 6729−6740.

(3) Li, G.; Li, L.; Feng, S.; Wang, M.; Zhang, L.; Yao, X. Edge-Epitaxial Growth of 2D NbS2-WS2 Lateral Metal-Semiconductor Heterostructures. *Adv. Mater.* **1999**, *11*, 146−149.

(4) Feng, S.; Greenblatt, M. Effect of iodine intercalation on superconductivity in the Bi-Sr-Ca-Cu-O system. *Chem. Mater.* **1992**, *4*, 1257−1262.

(5) Chen, Q. W.; Qian, Y. T.; Chen, Z. Y.; Tang, K. B.; Zhou, G. E.; Zhang, Y. H. Superconductivity in the Bi-Sr-Ca-Cu-O System. *Phys. C* **1994**, *224*, 228−230.

(6) Zhao, C.; Feng, S.; Xu, R.; Shi, C.; Ni, J. Hydrothermal synthesis and lanthanide doping of complex fluorides, LiYF$_4$, KYF$_4$ and BaBeF$_4$ under mild conditions. *Chem. Commun.* **1997**, *10*, 945−946, DOI: 10.1039/A607066C.

(7) Feng, S.; Wang, D.; Yu, R.; N, L. Hydrothermal synthesis and network structure of [[Ni$_4$(male)$_4$(m-4-ClPh)$_4$].CH$_3$OH].CH$_3$OH. - Proceedings and undefined *Solvothermal Technol. Res. Tak.* **1997**.

(8) Derbel, M. A.; Turnbull, M. M.; Naïli, H.; Rekik, W. Supramolecular assembly of a novel manganese(II) complex: Structural characterization, DFT study, Hirshfeld surface analysis and solvent effect. *Polyhedron* **2020**, *175*, No. 114220.

(9) Jlassi, R.; Ribeiro, A. P. C.; Alegria, E. C. B. A.; Naïli, H.; Tiago, G. A. O.; Rüffer, T.; Lang, H.; Zubkov, F. I.; Pombeiro, A. J. L.; Rekik, W. Synthesis, crystal structure, and antimicrobial activity of new copper(II) complexes with 3,5-dimethylpyrazole and carboxylate co-ligands. *Inorg. Chim. Acta* **2018**, *471*, 658−663.

(10) Moghdad, I.; Mbarek, A.; Costantino, F.; Nazzareni, S.; Naïli, H. Synthesis, characterization, and DFT study of new palladium(II) and platinum(II) complexes with 4-aryl-5-(pyridin-4-yl)-4H-1,2,4-triazole-3-thiols. *J. Mol. Struct.* **2020**, *1202*, No. 127326.

(11) Saïd, S.; Kolsi, R. B. A.; Naïli, H. Exploring Organometallic Chemistry: Synthesis and Characterization of New Ruthenium(II) Complexes with Pyridyl-Substituted Alkynes. *J. Organomet. Chem.* **2016**, *809*, 45−56.

(12) Hfidhi, N.; Korb, M.; Fitta, M.; Čižmár, E.; Lang, H.; Naïli, H. Synthesis and Structural Characterization of Novel Manganese(II) Complexes with Tridentate Ligands. *Inorg. Chim. Acta* **2019**, *484*, 206−213.

(13) Dgachi, S.; Rahmouni, F.; Soran, A.; Saoudi, M.; Nemes, G.; Naïli, H. Investigating the Molecular Structures and Spectroscopic Properties of New Palladium(II) and Platinum(II) Complexes. *J. Mol. Struct.* **2021**, *1244*, No. 130996.

(14) Sayer, I.; Dege, N.; Ghalla, H.; Moliterni, A.; Naïli, H. Supramolecular Assemblies of Copper(I) Complexes with Aromatic Ligands: Synthesis, Characterization, and Theoretical Insights. *J. Mol. Struct.* **2021**, *1224*, No. 129266.

(15) Jlassi, R.; Khalladi, A.; Naïli, H.; Rüffer, T.; Lang, H.; Rekik, W. Synthesis and Structural Analysis of Novel Copper(II) Complexes with Pyrazole Derivatives. *Polyhedron* **2019**, *158*, 71−75.

(16) Hfidhi, N.; Kammoun, O.; Pelka, R.; Fitta, M.; Naïli, H. Exploring the Coordination Chemistry of Copper(II) with Pyrazole-Based Ligands: Synthesis and Structural Characterization. *Inorg. Chim. Acta* **2018**, *469*, 431−439.

(17) Da Silva, V. S.; Meireles, A. M.; Da Silva Martins, D. C.; Rebouças, J. S.; Defreitas-Silva, G.; Idemori, Y. M. Investigating the Catalytic Activity of New Palladium(II) Complexes in Olefin Oxidation. *Appl. Catal., A* **2015**, *491*, 17−27.

(18) Abdelhamid, H. N.; Mathew, A. P. Biopolymer-Based Adsorbents for Heavy Metal Ion Removal: A Review. *Carbohydr. Polym.* **2021**, *274*, No. 118657.

(19) Zhang, L. M.; Li, H. Y.; Li, H. X.; Young, D. J.; Wang, Y.; Lang, J. P. Design and Synthesis of Metal−Organic Frameworks for Gas Separation and Catalysis. *Inorg. Chem.* **2017**, *56*, 11230−11243.

(20) Zurowska, B.; Mroziński, J.; Julve, M.; Lloret, F.; Maslejova, A.; Sawka-Dobrowolska, W. Magnetostructural Correlations in a Family of Octanuclear [Mn(III)(μ_3-O)(RO)$_2$(HL)$_2$]$^{2+}$ Complexes. *Inorg. Chem.* **2002**, *41*, 1771−1777.

(21) Chang, X. H.; Qin, J. H.; Han, M. L.; Ma, L. F.; Wang, L. Y. Synthesis and Crystal Engineering of Novel Coordination Polymers Based on Flexible Multicarboxylate Ligands. *CrystEngComm* **2014**, *16*, 870−882.

(22) Wang, F.; Ke, X.; Zhao, J.; Deng, K.; Leng, X.; Tian, Z.; Wen, L.; Li, D. Design and Synthesis of Luminescent Coordination Polymers with Tetrazolate Ligands. *Dalton Trans.* **2011**, *40*, 11856−11865.

(23) Neese, F.; Wennmohs, F.; Becker, U.; Riplinger, C. Theoretical Approaches to Investigate Reaction Mechanisms in Bioinorganic Chemistry. *J. Chem. Phys.* **2020**, *152*, No. 224108.

(24) Neese, F. The ORCA Program System. *J. Chem. Phys.* **2007**, *127*, No. 164112.

(25) Angeli, C.; Borini, S.; Cestari, M.; Cimiraglia, R. Ab Initio Calculations of Hyperpolarizabilities and Second Hyperpolarizabilities of Nitroaromatics: A Four-Component Relativistic Approach. *J. Chem. Phys.* **2004**, *121*, 4043.

(26) Angeli, C.; Cimiraglia, R.; Malrieu, J. P. Many-body approaches using the Density Matrix Renormalization Group: a unified software presentation. *J. Chem. Phys.* **2002**, *117*, 9138.

(27) Angeli, C.; Cimiraglia, R.; Evangelisti, S.; Leininger, T.; Malrieu, J. P. Introduction of a density matrix renormalization group algorithm in the COLUMBUS multireference configuration inter-action code. *J. Chem. Phys.* **2001**, *114*, 10252.

(28) Atanasov, M.; Ganyushin, D.; Pantazis, D. A.; Sivalingam, K.; Neese, F. Orbital-interaction analysis of the magnetic anisotropy in trigonal bipyramidal Ni(II) complexes. *Inorg. Chem.* **2011**, *50*, 7460−7477.

(29) Ganyushin, D.; Neese, F. Efficient evaluation of spin−spin contributions to hyperfine coupling constants at the coupled cluster level of theory. *J. Chem. Phys.* **2006**, *125*, No. 024103.

(30) Neese, F. Prediction of molecular properties and molecular spectroscopy with density functional theory: From fundamental theory to exchange-coupling. *J. Chem. Phys.* **2005**, *122*, No. 034107.

(31) Maurice, R.; Bastardis, R.; de Graaf, C.; Suaud, N.; Mallah, T.; Gui-héry, N. Spin Hamiltonian Parameters from Density Functional Theory (DFT) Calculations: A Modular Software Suite. *J. Chem. Theory Comput.* **2009**, *5*, 2977−2984.

(32) Van Wüllen, C. Self-consistent implementation of the projector augmented-wave method: Application to the Si(111) surface. *J. Chem. Phys.* **1998**, *109*, 392.

(33) van Lenthe, E.; Baerends, E. J.; Snijders, J. G. Relativistic regular two-component Hamiltonians. *J. Chem. Phys.* **1998**, *99*, 4597−4610, DOI: 10.1063/1.466059.

(34) Schäfer, A.; Huber, C.; Ahlrichs, R. Fully optimized contracted Gaussian basis sets of triple zeta valence quality for atoms Li to Kr. *J. Chem. Phys.* **1998**, *100*, 5829−5835, DOI: 10.1063/1.467146.

(35) Neese, F.; Wennmohs, F.; Hansen, A.; Becker, U. Efficient, approximate and parallel Hartree−Fock and hybrid DFT calculations. A 'chain-of-spheres' algorithm for the Hartree−Fock exchange. *Chem. Phys.* **2009**, *356*, 98−109.

(36) Hellweg, A.; Hättig, C.; Höfener, S.; Klopper, W. A new local density functional for main-group thermochemistry, transition metal bonding, thermochemical kinetics, and noncovalent interactions. *Theor. Chem. Acc.* **2007**, *117*, 587−597.

(37) Weigend, F. Accurate Coulomb-fitting basis sets for H to Rn. *Phys. Chem. Chem. Phys.* **2006**, *8*, 1057−1065.

(38) Grimme, S.; Ehrlich, S.; Goerigk, L. A consistent and accurate ab initio parametrization of density functional dispersion correction (DFT-D) for the 94 elements H-Pu. *J. Comput. Chem.* **2011**, *32*, 1456−1465.

(39) Grimme, S.; Ehrlich, S.; Goerigk, L. A consistent and accurate ab initio parametrization of density functional dispersion correction (DFT-D) for the 94 elements H-Pu. *J. Chem. Phys.* **2010**, *132*, No. 154104, DOI: 10.1063/1.3382344.

(40) Farrugia, L. J. ORTEP-3 for Windows − a version of ORTEP-III with a graphical user interface (GUI). *J. Appl. Crystallogr.* **1999**, *32*, 837−838.

(41) Brandenburg, K. Diamond: A Crystal and Molecular Structure Visualization System *J. Appl. Crystallogr.* 2012.

(42) Wolff, S.; Grimwood, D.; McKinnon, M. T.-C.; CrystalExplorer17. *Crystal Impact GbR*. Australia, 2012.

(43) Hachuła, B.; Nowak, M.; Kusz, J. Synthesis and structure of diphosphine adducts of copper(I) complexes with organoarsenic ligands. *J. Chem. Crystallogr.* **2010**, *40*, 201−206.

(44) Goodgame, D. M. L.; Goodgame, M.; Rayner-Canham, G. W. The crystal structure of cobalt(II) cycloheptanecarboxylate. *Inorg. Chim. Acta* **1969**, *3*, 406−410.

(45) Perakis, F.; De Marco, L.; Shalit, A.; Tang, F.; Kann, Z. R.; Kühne, T. D.; Torre, R.; Bonn, M.; Nagata, Y. The formation and dynamics of hydrogen-bonded cages: A combined 2D-IR and Monte Carlo simulation study. *Chem. Rev.* **2016**, *116*, 7590−7607.

(46) Krushna, C.; Mohapatra, C.; Dash, K. C. Effect of Some Electrolytes on the Viscosities of Aqueous Solutions of N-Methylpyrrolidinone. *J. Inorg. Nucl. Chem.* **1977**, *39*, 1253−1258.

(47) Vlaicu, I. D.; Olar, R.; Scăeţeanu, G. V.; Silvestro, L.; Maurer, M.; Stănică, N.; Badea, M. Synthesis, crystal structure, Hirshfeld surface analysis, and DFT studies of two new palladium(II) complexes with 3,5-dimethylpyrazole. *J. Therm. Anal. Calorim.* **2018**, *134*, 503−512.

(48) Ishak, N. N. M.; Jamsari, J.; Ismail, A. Z.; Tahir, M. I. M.; Tie-kink, E. R. T.; Veerakumarasivam, A.; Ravoof, T. B. S. A. Synthesis, characterization, and DFT studies of new heterocyclic chalcone derivatives with potential biological activity. *J. Mol. Struct.* **2019**, *1198*, No. 126888.

(49) Ranga Rao, G.; Sahu, H. R. Microwave-assisted synthesis and spectral studies on some Co(II) complexes derived from 2,6-diacetylpyridine. *J. Chem. Sci.* **2001**, *113*, 651−658.

(50) Escobedo Morales, U. P. A.; Sanchez Mora, E. A novel catalyst based on a 4-[(N-carboxy)alkylamino]pyridine ligand for the telomerization of butadiene with methanol. *Rev. Mex. F'Isica* **2007**, *53*, 18−22.

(51) Dobrzynska, D.; Jerzykiewicz, L. B.; Duczmal, M.; Wojciechowska, A.; Jablonska, K.; Palus, J.; Ozarowski, A. Structure and Magnetic Properties of Dinuclear and Chain Complexes of Copper(II) with Pyrazole and Its Derivatives. *Inorg. Chem.* **2006**, *45*, 10479−10486.

(52) Gulcan, M.; Karataş, Y.; Işık, S.; Öztürk, G.; Akbaş, E.; Şahin, E. Synthesis and Photophysical Properties of Benzimidazole Derivatives Bearing Pyrene Moieties. *J. Fluoresc.* **2014**, *24*, 1679−1686.

(53) Gao, L.; Wang, F.; Zhao, Q.; Zhang, Y.; Dong, W. K. Synthesis, Crystal Structure, and Magnetic Properties of a 3D Coordination Polymer Based on 5-Methylisophthalic Acid. *Polyhedron* **2018**, *139*, 7−16.

(54) Schweinfurth, D.; Krzystek, J.; Schapiro, I.; Demeshko, S.; Klein, J.; Telser, J.; Ozarowski, A.; Su, C. Y.; Meyer, F.; Atanasov, M.; Neese, F.; Sarkar, B. Electronic Structure of Bispidine Copper (II) Complexes. *Inorg. Chem.* **2013**, *52*, 6880−6892.

(55) Vermaas, A.; Groeneveld, W. L.; Reedijk, J. (1977). "Structure of Tetranuclear Copper (II) Pyrazolate Complexes. *Z. Naturforsch. A* **1977**, *32*, 632−640.

(56) Merriam, J. S.; Perumareddi, J. R. Metal-Ligand Bond Lengths and Force Constants. I. A Conformational Study of 2-Formylpyridine Thiosemicarbazone and Its Metal Complexes. *J. Phys. Chem. A* **1975**, *79*, 142−149.

(57) Dobrzyńska, D.; Jerzykiewicz, L. B.; Duczmal, M.; Wojciechowska, A.; Jabłońska, K.; Palus, J.; Ozarowski, A. Structure and Magnetic Properties of Dinuclear and Chain Complexes of Copper (II) with Pyrazole and Its Derivatives. *Inorg. Chem.* **2006**, *45*, 10479−10486.

(58) Zawal, P.; Sen, H.; Klejna, S.; Mazur, T.; Wlaz, E.; Szaciłowski, K. Unraveling the Structure-Activity Relationship in Ru (II) Polypyridyl Complexes Containing 1,3,5-Triphenylbenzene Ligands. *Coord. Chem. Rev.* **2020**, *415*, No. 213316.

(59) Wang, J.; Liu, Y.; Han, S.; Li, Y.; Xu, Z.; Luo, J.; Hong, M.; Sun, Z. Surface-State-Enhanced Raman Scattering of Molecular Adsorbates on Transition Metal Dichalcogenides. *Sci. Bull.* **2020**, *66*, 158−163.

(60) Msalmi, R.; Elleuch, S.; Hamdi, B.; Abd El-Fattah, W.; Ben Hamadi, N.; Naili, H. A New Bipyridine-Phenolate Cu(II) Complex: Synthesis, Characterization, and Catalytic Activity towards the Degradation of Methylene Blue. *RSC Adv.* **2022**, *12*, 10431.

(61) Subbiah, A.; Sambamoorthy, S. Studies on the Reactivity of Bis(dimethylamino)phosphanyl Radical towards Isocyanates: Syn-

thesis and Characterization of Phosphinine-Appended Carbodiimide and Diaminocarbene. *Orient. J. Chem.* **2018**, *34,* 2008.

(62) Šterbinská, S.; Holub, M.; Kuchár, J.; Čižmár, E.; Černák, J. Synthesis and characterization of coordination compounds of ruthenium (II) with mixed ligands. *Polyhedron* **2020**, *187*, 114.

(63) Manson, J. L.; Manson, Z. E.; Sargent, A.; Villa, D. Y.; Etten, N. L.; Blackmore, W. J. A.; Curley, S. P. M.; Williams, R. C.; Brambleby, J.; Goddard, P. A.; Ozarowski, A.; Wilson, M. N.; Huddart, B. M.; Lancaster, T.; Johnson, R. D.; Blundell, S. J.; Bendix, J.; Wheeler, K. A.; Lapidus, S. H.; Xiao, F.; Birnbaum, S.; Singleton, J. Magnetic Frustration and Quantum Criticality in a New Kagome Antiferromagnet. *Polyhedron.* **2020**, *180*, No. 114379.

(64) Blackmore, W. J. A.; Brambleby, J.; Lancaster, T.; Clark, S. J.; Johnson, R. D.; Singleton, J.; Ozarowski, A.; Schlueter, J. A.; Chen, Y. S.; Arif, A. M.; Lapidus, S.; Xiao, F.; Williams, R. C.; Blundell, S. J.; Pearce, M. J.; Lees, M. R.; Manuel, P.; Villa, D. Y. A.; Villa, J. A.; Manson, J. L.; Goddard, P. A. Magnetic Frustration and Quantum Criticality in a New Kagome Antiferromagnet. *New J. Phys.* **2019**, *21*, No. 093025.

(65) Fisher, M. E. Renormalization Group Theory: Its Basis and Formulation in Statistical Physics. *Am. J. Phys.* **1964**, *32*, 343.